

# Electrostatically Directed Assembly of Nanostructured Composites for Enhanced Photocatalysis

Sebastian Kohsakowski, Petra Pulisova, Dariusz Mitoraj, Susann Neubert, Johannes Biskupek, Ute Kaiser, Sven Reichenberger, Galina Marzun, and Radim Beranek\*

It is well established that the activity of photocatalysts can be improved by deposition of redox catalysts, which can effectively extract the photogenerated charge carriers, enhance the rate of interfacial reactions, and thus suppress undesired recombination processes. For optimum performance, a high degree of control over the loading, size, and surface catalytic properties of redox catalyst particles is desirable. Herein, a novel, highly controllable, and versatile method for preparation of TiO<sub>2</sub> catalyst composites is reported. It starts with the generation of “naked” (ligand-free) nanoparticles of CuO<sub>x</sub> or FeO<sub>x</sub> by pulsed laser ablation of metal oxide targets in water. In the next step, a nearly quantitative colloidal deposition of CuO<sub>x</sub> and FeO<sub>x</sub> nanoparticles onto anatase TiO<sub>2</sub> substrate is achieved by adjusting the pH in order to establish electrostatic attraction between the colloids and the substrate. The resulting TiO<sub>2</sub>–CuO<sub>x</sub> and TiO<sub>2</sub>–FeO<sub>x</sub> assemblies with optimum catalyst amount (≈0.5 wt%) exhibit photocatalytic rates in degradation of 2,4-dichlorophenoxyacetic acid enhanced by a factor of ≈1.5 as compared to pristine TiO<sub>2</sub> under simulated solar irradiation. The electrostatically directed assembly of TiO<sub>2</sub> with ligand-free catalyst nanoparticles generated by pulsed laser ablation is thus demonstrated as a viable tool for preparation of composites with enhanced photocatalytic performance.

improved by deposition of redox catalysts, which can effectively extract the photogenerated charge carriers, improve the rate of interfacial electron and/or hole transfers, and thus suppress undesired recombination processes.<sup>[2]</sup> In case of photocatalytic degradation of organic pollutants, this approach has been in particular motivated by the need to enhance the kinetics of dioxygen reduction by photogenerated electrons since this reaction represents typically the rate-limiting step in the photodegradation process. This has already been suggested by Gerischer and Heller in the 1990s,<sup>[3]</sup> and later confirmed by kinetic studies using transient absorption spectroscopy that have demonstrated that the reduction of dioxygen by photogenerated electrons occurs on a much longer time-scale (microseconds) than, for example, the oxidation of alcohols by photogenerated holes (nanoseconds).<sup>[4]</sup> Indeed, significant enhancements of photocatalytic degradation rates have been, for example, demonstrated for TiO<sub>2</sub> photocatalysts modified by Pt,<sup>[3a,5]</sup> CuO<sub>x</sub>, and FeO<sub>x</sub> nanoparticles,<sup>[6]</sup> or even with isolated single Cu(II) and Fe(III) ions.<sup>[7]</sup> It is important to realize that a high degree of control over the loading, size, and surface catalytic properties of the redox catalyst particles is highly desirable in order to tune the resulting composites for optimum performance.<sup>[8]</sup> In this context, it is not surprising that mostly employed methods of preparation of photocatalytic composites have been impregnation<sup>[6a–d,9]</sup> and deposition precipitation,<sup>[3a,5,6e,f]</sup> since


## 1. Introduction

Sunlight-driven heterogeneous photocatalysis is potentially one of the most attractive approaches for driving useful chemical transformations like hydrogen evolution from water or decontamination of water or air from toxic organic pollutants.<sup>[1]</sup> It is well established that the activity of typical semiconductor photocatalysts (e.g., TiO<sub>2</sub>, SrTiO<sub>3</sub>, CdS, BiVO<sub>4</sub>, etc.) can be significantly

improved by deposition of redox catalysts, which can effectively extract the photogenerated charge carriers, improve the rate of interfacial electron and/or hole transfers, and thus suppress undesired recombination processes.<sup>[2]</sup> In case of photocatalytic degradation of organic pollutants, this approach has been in particular motivated by the need to enhance the kinetics of dioxygen reduction by photogenerated electrons since this reaction represents typically the rate-limiting step in the photodegradation process. This has already been suggested by Gerischer and Heller in the 1990s,<sup>[3]</sup> and later confirmed by kinetic studies using transient absorption spectroscopy that have demonstrated that the reduction of dioxygen by photogenerated electrons occurs on a much longer time-scale (microseconds) than, for example, the oxidation of alcohols by photogenerated holes (nanoseconds).<sup>[4]</sup> Indeed, significant enhancements of photocatalytic degradation rates have been, for example, demonstrated for TiO<sub>2</sub> photocatalysts modified by Pt,<sup>[3a,5]</sup> CuO<sub>x</sub>, and FeO<sub>x</sub> nanoparticles,<sup>[6]</sup> or even with isolated single Cu(II) and Fe(III) ions.<sup>[7]</sup> It is important to realize that a high degree of control over the loading, size, and surface catalytic properties of the redox catalyst particles is highly desirable in order to tune the resulting composites for optimum performance.<sup>[8]</sup> In this context, it is not surprising that mostly employed methods of preparation of photocatalytic composites have been impregnation<sup>[6a–d,9]</sup> and deposition precipitation,<sup>[3a,5,6e,f]</sup> since

S. Kohsakowski, Dr. S. Reichenberger, Dr. G. Marzun  
Technical Chemistry I and Center of Nanointegration  
Duisburg-Essen (CENIDE)  
University of Duisburg-Essen  
Universitätsstraße 7, 45141 Essen, Germany  
S. Kohsakowski, Dr. S. Reichenberger, Dr. G. Marzun  
NanoEnergieTechnikZentrum (NETZ)  
Carl-Benz-Straße 199, 47057 Duisburg, Germany

Dr. P. Pulisova, Dr. S. Neubert  
Faculty of Chemistry and Biochemistry  
Ruhr University Bochum  
Universitätsstraße 150, 44801 Bochum, Germany  
Dr. D. Mitoraj, Prof. R. Beranek  
Institute of Electrochemistry  
Ulm University  
Albert-Einstein-Allee 47, 89081 Ulm, Germany  
E-mail: radim.beranek@uni-ulm.de  
Dr. J. Biskupek, Prof. U. Kaiser  
Electron Microscopy of Materials Science  
Central Facility for Electron Microscopy  
Ulm University  
Albert-Einstein-Allee 11, 89081 Ulm, Germany

 The ORCID identification number(s) for the author(s) of this article can be found under <https://doi.org/10.1002/smt.201800390>.

DOI: 10.1002/smt.201800390

these methods typically do not require the use of stabilizing surfactants (capping agents) that might interfere with the catalytic behavior of redox catalysts and cannot be always easily removed without heat treatment steps compromising the catalytic efficiency. On the other hand, colloidal deposition of preformed colloids allows for a higher degree of control over the size and loading of catalyst nanoparticles, yet often requires the use of additional stabilizing ligands.

Inspired by the above-mentioned recent progress in use of Cu(II)- and Fe(III)-based redox catalysts,<sup>[6,7]</sup> we report a novel and highly controllable method for preparation of TiO<sub>2</sub> catalyst composites based on electrostatically driven colloidal deposition of “naked” (no stabilizing capping agents) nanoparticles of CuO<sub>x</sub> or FeO<sub>x</sub> onto TiO<sub>2</sub> powder substrates. The ligand-free nanoparticles are generated in water by pulsed laser ablation, which is a well-established and highly versatile method for controlled synthesis of colloids with a high throughput.<sup>[10]</sup> Furthermore, we provide a simple protocol for a nearly quantitative colloidal deposition of CuO<sub>x</sub> and FeO<sub>x</sub> redox catalysts onto anatase TiO<sub>2</sub> substrate, demonstrate photocatalytic degradation rates enhanced by a factor of 1.5 upon deposition of redox catalysts under optimized conditions, and discuss the mechanism of the enhancement.

## 2. Results and Discussion

Previously, CuO<sub>x</sub> or FeO<sub>x</sub> nanoparticles have been shown to be generated along with metallic nanoparticles by laser ablation of pure copper or iron metal targets or by laser fragmentation of micropowders in different liquids.<sup>[10a,e,11]</sup> Herein, we use CuO<sub>x</sub> and FeO<sub>x</sub> pressed powder ablation targets to directly generate metal oxide nanoparticles. In order to generate the colloidal CuO<sub>x</sub> and FeO<sub>x</sub> nanoparticles (Figure 1), we used a nanosecond laser system and a continuous ablation flow chamber with pure water as a solvent. The production rate of CuO<sub>x</sub> and FeO<sub>x</sub> colloidal particles in our laser ablation system was ≈200–300 mg h<sup>-1</sup>. The size distribution of colloids was analyzed through differential centrifugal sedimentation. The average hydrodynamical particle size of CuO<sub>x</sub> and FeO<sub>x</sub> nanoparticles was 43 and 38 nm, respectively (Figure S1, Supporting Information). These results are in line with transmission electron microscopy (TEM) analysis, which also shows that FeO<sub>x</sub> nanoparticles are nearly spherical and the CuO<sub>x</sub> nanoparticles have an elongated shape (Figure S2, Supporting Information). The powder X-ray diffraction (XRD) patterns confirmed the presence of crystalline CuO (Figure S3, Supporting Information). In contrast, no reflexes of crystalline Fe<sub>2</sub>O<sub>3</sub> have been detected, suggesting a mostly disordered, mixed-phase, and/or amorphous structure of FeO<sub>x</sub> nanoparticles. As it is well known that laser ablation of metal oxides may lead to formation of nonstoichiometric phases and/or amorphous side products,<sup>[10c]</sup> we choose to designate our colloids as “CuO<sub>x</sub>” and “FeO<sub>x</sub>”.

The CuO<sub>x</sub> and FeO<sub>x</sub> colloidal nanoparticles were deposited onto anatase titanium dioxide (TiO<sub>2</sub>(A)) powder consisting of ≈0.2–1 μm sized aggregates of much smaller

(average size of ≈15 nm as determined by the Scherrer formula) crystallites (Figure S4, Supporting Information).

In order to establish a protocol for effective colloidal deposition, we first determined the isoelectric points (IEPs) of the colloids and the TiO<sub>2</sub>(A) substrate by zeta potential measurements (Figure 2a). It is known that efficient electrostatically driven particle adsorption takes place if the pH is between the IEPs of the colloidal nanoparticles and the support.<sup>[12]</sup> This strategy has been, for example, employed for fabrication of photoactive heterojunctions from two different light absorbers.<sup>[13]</sup> Based on the obtained IEP values, the pH value of the colloidal solutions and the TiO<sub>2</sub>(A) substrate suspension was adjusted to 6 before mixing, since at this pH the net surface charge is negative for TiO<sub>2</sub>(A) but positive for both CuO<sub>x</sub> and FeO<sub>x</sub> colloids (Figure 2b). We anticipated that the attractive electrostatic interaction between the substrate TiO<sub>2</sub>(A) and the redox catalyst colloids should enable highly quantitative colloidal deposition. Indeed, the loading efficiency determined by differential UV–vis spectroscopy was 95–99% for both colloidal catalysts, which allows for an excellent control over the actual loading of the redox catalyst simply by adjusting the concentration of colloidal nanoparticles in the deposition solution (Table 1).

The resulting composites were slightly grayish or brownish in case of TiO<sub>2</sub>(A)–CuO<sub>x</sub> and TiO<sub>2</sub>(A)–FeO<sub>x</sub>, respectively. Their electronic absorption properties were still dominated by the fundamental band-to-band transition at 3.2 eV (≈390 nm) corresponding to the bandgap of anatase TiO<sub>2</sub> (Figure S5, Supporting Information), and the presence of CuO<sub>x</sub> and FeO<sub>x</sub> led only to very weak and broad absorption shoulders in the visible range. In addition, the presence of Cu and Fe in the resulting composites was confirmed by energy-dispersive X-ray (EDX) spectroscopy (Figure S6, Supporting Information). Direct TEM visualization of CuO<sub>x</sub> and FeO<sub>x</sub> catalyst nanoparticles in TiO<sub>2</sub>(A) powders turned out to be rather challenging due to very small content of the catalysts. However, in case of highly loaded TiO<sub>2</sub>(A)–FeO<sub>x</sub>, we succeeded to display a FeO<sub>x</sub> nanoparticle (size of ≈35 nm) embedded into TiO<sub>2</sub>(A) matrix by energy-filtering TEM (EFTEM) mapping with electron energy loss spectroscopy (EELS) elemental detection (Figure 2c,d). This suggests that the colloidal deposition leads to random and uniform distribution of redox catalyst particles on the surface of TiO<sub>2</sub> without significant agglomeration.

To ensure that CuO<sub>x</sub> and FeO<sub>x</sub> nanoparticles formed by pulsed laser ablation of the respective pressed oxide powders were present on the TiO<sub>2</sub> after colloidal deposition, X-ray photoelectron spectroscopy (XPS) measurements of nominally

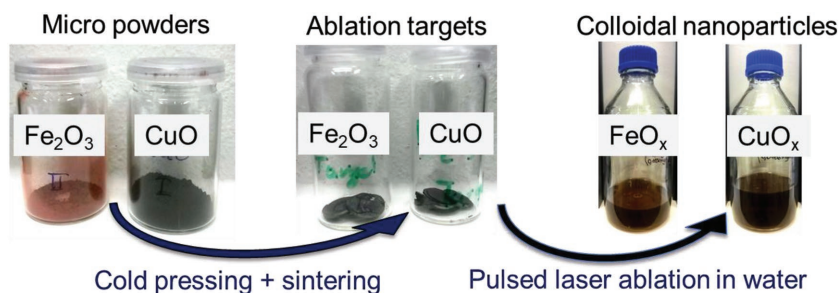


**Figure 1.** Colloidal solutions of CuO<sub>x</sub> and FeO<sub>x</sub> nanoparticles were prepared by pulsed laser ablation of CuO and Fe<sub>2</sub>O<sub>3</sub> targets in water.

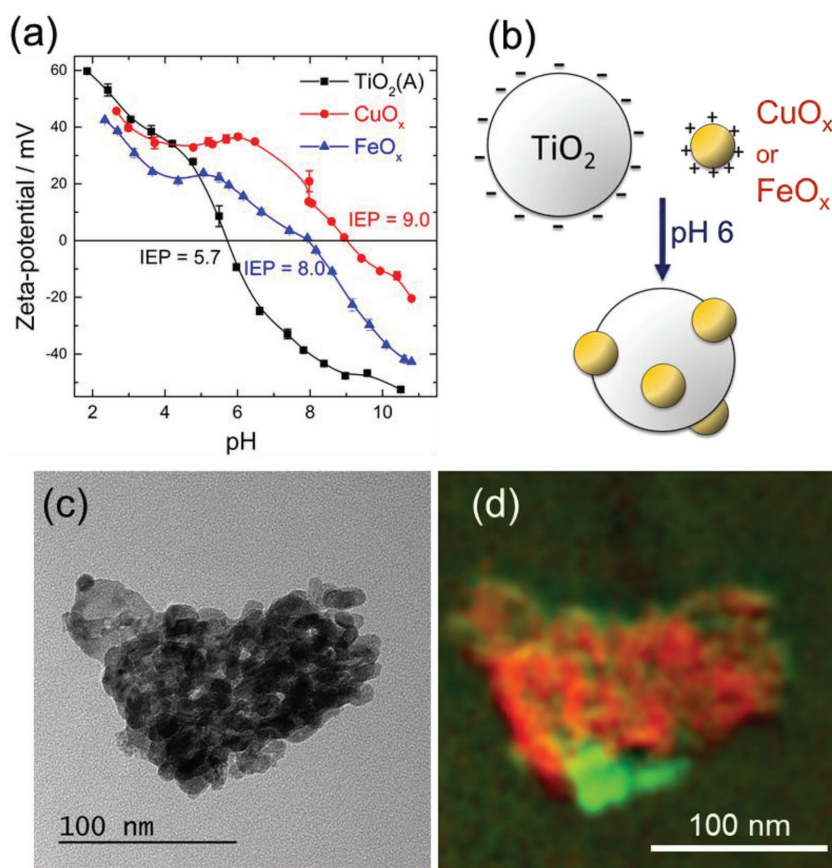


**Figure 2.** a) IEP measurements of colloidal solutions of  $\text{CuO}_x$  and  $\text{FeO}_x$  nanoparticles prepared by pulsed laser ablation of  $\text{CuO}$  and  $\text{Fe}_2\text{O}_3$  targets in water; b) electrostatically driven colloidal deposition of  $\text{CuO}_x$  and  $\text{FeO}_x$ . Elemental mapping using EFTEM: c) zero-loss filtered overview image of  $\text{TiO}_2(\text{A})$ - $\text{FeO}_x$  (4.57 wt%) showing the agglomerated particles; d) a superimposed map (Fe green channel using the  $\text{Fe}_{2,3}$  edge, Ti red channel using the  $\text{Ti}_{2,3}$  edge) shows the  $\text{FeO}_x$  distribution within the composite.

5 wt% loaded samples were conducted. The results are summarized in Figure S7 (Supporting Information) for three different measurement positions. Since the  $\text{FeO}_x$  and  $\text{CuO}_x$  nanoparticles are embedded into the porous structure of larger  $\text{TiO}_2$  aggregates and due to the rather large particle size of  $\approx 35$ – $50$  nm for both  $\text{FeO}_x$  and  $\text{CuO}_x$  nanoparticles and the consequently low surface area, the overall peak intensities of iron and copper signals were very low considering the weight loading is already  $\approx 5$  wt% ( $\approx 5 \times 10^4$  ppm). In case of the  $\text{FeO}_x$  sample, the  $2p_{3/2}$  peak is clearly shifted by about 3 eV toward higher binding energies (BEs) with respect to pure iron (BE  $\approx 706.3$  eV),<sup>[14]</sup> indicating the presence of oxidized iron. Furthermore, satellite peaks known to occur if iron oxide is found in the range between 716 and 719 eV.<sup>[14]</sup> From deconvolution of the XPS data and comparing the peak areas,  $\approx 75$ – $80\%$  of surface iron is present as  $\text{Fe(III)}$  with the rest remaining as  $\text{Fe(II)}$ . In case of  $\text{CuO}_x$  nanoparticles supported on  $\text{TiO}_2$  (Figure S7, Supporting Information, right column), detecting oxidized copper species is not straightforward since Cu and  $\text{Cu}_2\text{O}$  do not obtain significant peak splitting (considering the energy resolution error of the measurement  $\approx 0.3$  eV) and the peak shift of  $\text{CuO}$  is +1 eV with respect to elemental copper signal.<sup>[15]</sup> Following the deconvolution,  $\approx 30$ – $40\%$  of the detected copper atoms are

present as  $\text{CuO}$ , while the remaining 60–70% are either Cu or  $\text{Cu}_2\text{O}$ . Due to the low intensity of the signal, satellite peaks often used as characteristic for  $\text{Cu(II)}$  are not or only barely visible. Yet, it is known from studies on the oxidizing behavior of pulsed laser ablation that ablation of copper in water leads to significant formation of copper oxide species as reported by Marzun et al.<sup>[10e]</sup> Generally, the occurrence of surface oxidation is reported in numerous studies on pulsed laser ablation in liquid (even for gold) and is considered an important factor for the possibility to electrostatically stabilize the surfactant-free nanoparticles by adjusting the pH such that, e.g.,  $\text{M-O}^-$  surfaces are present. The latter has been comprehensively reviewed by Zhang et al.<sup>[10c]</sup> By means of plasma spectroscopy, the reformation of  $\text{Al}_2\text{O}_3$  during ablation of an  $\text{Al}_2\text{O}_3$  target was studied by Lam et al. modeling the reformation of the oxide from the plasma and underlining that the oxidation state is maintained during ablation of fully oxidized materials.<sup>[16]</sup> Consequently, the observed  $\text{Fe(III)}$  and  $\text{Cu(II)}$  species in XPS are in good agreement and indicate the presence of  $\text{FeO}_x$  and  $\text{CuO}_x$  nanoparticles on  $\text{TiO}_2$ , respectively.

In order to find the optimum loading for the photocatalytic activity in photodegradation of 2,4-dichlorophenoxyacetic acid (2,4-D, herbicide) as a test pollutant, we performed a series of photodegradation experiments under simulated solar irradiation (Figure 3a).

Photocatalysts modified with  $\text{CuO}_x$  and  $\text{FeO}_x$  colloids with loadings up to 1 wt% exhibited enhanced photocatalytic degradation rates as compared to pristine  $\text{TiO}_2(\text{A})$  material. At lower loadings, the amount of  $\text{CuO}_x$  and  $\text{FeO}_x$  is too low and only a minor part of photogenerated electrons can be effectively transferred to the redox catalysts. At higher loadings, the

**Table 1.** Nominal (theoretical) and actual loading of redox catalysts.

Composite	Nominal loading [wt%]	Actual loading <sup>a)</sup> [wt%]
$\text{TiO}_2(\text{A})$ - $\text{CuO}_x$	0.050	0.047
$\text{TiO}_2(\text{A})$ - $\text{CuO}_x$	0.10	0.099
$\text{TiO}_2(\text{A})$ - $\text{CuO}_x$	0.50	0.49
$\text{TiO}_2(\text{A})$ - $\text{CuO}_x$	1.0	0.97
$\text{TiO}_2(\text{A})$ - $\text{CuO}_x$	5.00	4.92
$\text{TiO}_2(\text{A})$ - $\text{FeO}_x$	0.050	0.049
$\text{TiO}_2(\text{A})$ - $\text{FeO}_x$	0.10	0.099
$\text{TiO}_2(\text{A})$ - $\text{FeO}_x$	0.50	0.49
$\text{TiO}_2(\text{A})$ - $\text{FeO}_x$	1.0	0.98
$\text{TiO}_2(\text{A})$ - $\text{FeO}_x$	5.00	4.57

<sup>a)</sup>For the determination of actual loading, see the Experimental Section.



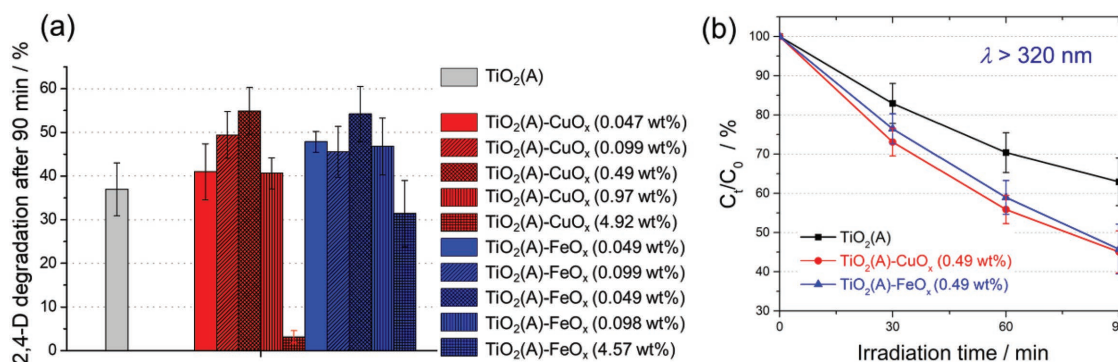


**Figure 3.** a) Comparison of 2,4-D degradation yields after 90 min of photocatalytic experiments using simulated sunlight ( $\lambda > 320$  nm) at pristine anatase TiO<sub>2</sub>(A) photocatalyst (gray), TiO<sub>2</sub>(A)-CuO<sub>x</sub> (red), and TiO<sub>2</sub>(A)-FeO<sub>x</sub> (blue) with different amounts of the redox catalyst (actual loading is given). b) Concentration changes of 2,4-D during photocatalytic degradation experiments using pristine anatase TiO<sub>2</sub>(A) and TiO<sub>2</sub>(A) loaded with optimum amounts (0.49 wt%) of CuO<sub>x</sub> or FeO<sub>x</sub> redox catalyst nanoparticles.

photoactivity decreased significantly, which can be clearly ascribed to the parasitic light absorption of the CuO<sub>x</sub> and FeO<sub>x</sub> redox catalysts. In other words, since CuO<sub>x</sub> and FeO<sub>x</sub> also absorb light in the UV range, larger amounts of the catalyst can absorb significant portion of UV light and thus block the light harvesting by TiO<sub>2</sub>(A). Therefore, in case of photo(electro) catalytic architectures comprising light absorbers and redox catalysts, there is typically an optimum loading of the catalyst that is adjusted by the trade-off between the enhancement of redox catalysis and blocking the light absorption.<sup>[17]</sup> In cases of both CuO<sub>x</sub> and FeO<sub>x</sub>, the best-performing composites had the actual loading of 0.49 wt%, whereby the photodegradation rates were enhanced by a factor of  $\approx 1.5$  as compared to pristine TiO<sub>2</sub>(A) (Figure 3b).

In line with previous results on Cu(II)- and Fe(III)-modified photocatalysts reported by us and others,<sup>[6,7,9]</sup> we assume that this enhanced photoactivity can be ascribed to effective interfacial transfer of photogenerated electrons from TiO<sub>2</sub> to CuO<sub>x</sub> and FeO<sub>x</sub>, thus directly improving the primary charge separation and allowing for more efficient reductive catalysis at the surface of redox catalysts (Figure 4).

Indeed, the efficient trapping of photogenerated electrons at CuO<sub>x</sub> and FeO<sub>x</sub> is corroborated by solid-state photoluminescence spectra (Figure 5) that show significant quenching of luminescence

in the presence of redox catalyst nanoparticles, indicating that the radiative recombination rate is diminished.

In this context, we note that dissolved dioxygen not only serves as an acceptor of photogenerated electrons during photodegradation, but can also become a source of other reactive oxidizing species (e.g., superoxide anion, hydrogen peroxide, or hydroxyl radical), which can play an active role in the degradation process. Therefore, the production of  $\cdot\text{OH}$  radicals was followed by recording fluorescence spectra of hydroxyterephthalic acid (TAOH) formed upon irradiation of the material suspensions in a terephthalic acid (TA) solution under irradiation (Figure 6). The production of hydroxyl radicals for each sample is proportional to the fluorescence intensity due to formation of hydroxyterephthalic acid.<sup>[18]</sup> Apparently, there is no straightforward correlation between  $\cdot\text{OH}$  radical production and photoactivity in degradation of 2,4-D. While TiO<sub>2</sub>(A)-FeO<sub>x</sub> exhibits the highest rate of  $\cdot\text{OH}$  radical production, the TiO<sub>2</sub>(A)-CuO<sub>x</sub> composite shows  $\cdot\text{OH}$  radical production rate lower by a factor of 2 as compared to pristine TiO<sub>2</sub>(A), though the degradation rates of 2,4-D were comparable in both cases (Figure 3). It should be noted that we recently observed very similar results in case of rutile

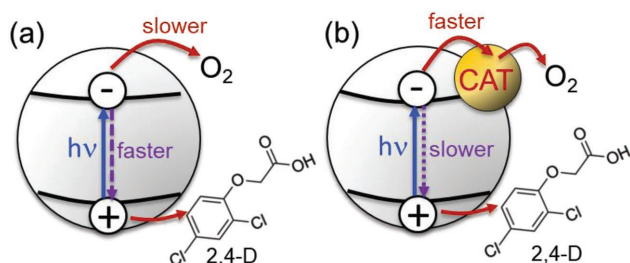


**Figure 4.** Simplified scheme showing the proposed mechanism of enhancement of photocatalytic activity by deposition of CuO<sub>x</sub> and FeO<sub>x</sub> redox catalysts: at pristine TiO<sub>2</sub> (a) the oxygen reduction is slower and the recombination of photogenerated electrons is faster than those in the presence of redox catalysts (b), which effectively extract the photogenerated electrons, rendering the oxygen reduction and charge separation more efficient and the recombination slower (b).

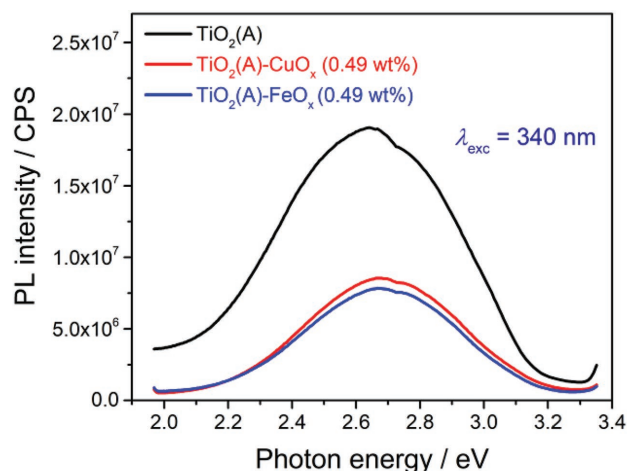


**Figure 5.** Solid-state photoluminescence spectra of TiO<sub>2</sub>(A), TiO<sub>2</sub>(A)-CuO<sub>x</sub>, and TiO<sub>2</sub>(A)-FeO<sub>x</sub>.

TiO<sub>2</sub> materials modified by isolated Cu(II) and Fe(III) ions.<sup>[7b]</sup> In general, our results suggest that while the primary charge separation is enhanced in the presence of both CuO<sub>x</sub> and FeO<sub>x</sub> (as evident from the photoluminescence quenching), the interfacial redox catalysis might be mechanistically slightly different in case of CuO<sub>x</sub> and FeO<sub>x</sub> redox catalysts. At TiO<sub>2</sub>(A)-CuO<sub>x</sub>, the role of •OH radical in the enhanced photooxidation of 2,4-D is clearly rather minor, and we assume that the photoactivity enhancement is mostly due to more efficient electron extraction and catalysis of primary dioxygen reduction.<sup>[7b]</sup> In contrast, in case of TiO<sub>2</sub>(A)-FeO<sub>x</sub>, the increased rate of •OH radical production cannot be ruled out as an important factor in activity enhancement. Since one can assume that the nature of photogenerated holes in all samples is the same, we hypothesize that the enhanced formation of •OH at TiO<sub>2</sub>(A)-FeO<sub>x</sub> has its origin in the reductive pathway that is initiated by reduction of dioxygen by photogenerated electrons. For example, it is known that hydrogen peroxide can be formed by a two-electron reduction of dioxygen catalyzed by Fe(III) surface catalytic sites of FeO<sub>x</sub>. The H<sub>2</sub>O<sub>2</sub> molecules thus formed can be subsequently converted to •OH radicals either via reduction by photogenerated electrons or by Fenton-type reactions involving reactions of Fe(II) and/or Fe(III) with H<sub>2</sub>O<sub>2</sub> under formation of •OH or hydroperoxyl (HOO•) radicals.

### 3. Conclusion

We demonstrate a simple and straightforward method for assembly of composite photocatalysts based on low-cost redox catalysts (CuO<sub>x</sub> and FeO<sub>x</sub>) supported on anatase TiO<sub>2</sub> via an electrostatically directed colloidal deposition. Our approach capitalizes on a novel, high-throughput fabrication of capping agent-free (“naked”) CuO<sub>x</sub> or FeO<sub>x</sub> colloids by pulsed laser ablation of metal oxide pressed powder targets in water. The colloidal deposition process onto anatase TiO<sub>2</sub>(A) support is shown to be easily controllable by adjusting the pH value,

achieving a nearly quantitative deposition under optimum conditions, and thus allowing a very precise control of the actual loading of redox catalysts, which is crucial for optimizing the photocatalytic performance. This method is very energy and materials efficient, does not require any use of organic solvents, and thus represents a viable “green” approach for fabrication of functional composite nanoarchitectures. Under optimized conditions, the resulting TiO<sub>2</sub>(A)-CuO<sub>x</sub> and TiO<sub>2</sub>(A)-FeO<sub>x</sub> photocatalytic composites exhibit enhancement by a factor of 1.5 in photodegradation of a test herbicide (2,4-D) as compared to pristine TiO<sub>2</sub>(A). Initial mechanistic investigations suggest that the improved photocatalytic performance is mainly due to more effective extraction of photogenerated electrons from TiO<sub>2</sub> to CuO<sub>x</sub> and FeO<sub>x</sub> redox catalysts, followed by catalysis of “dark” redox reactions at the photocatalyst surface. As the activity, selectivity, and stability of most photocatalysts are known to be highly substrate specific and depending also on a complex interplay between the material properties of the light absorber and surface catalysts,<sup>[2e,f,19]</sup> the method demonstrated here for tunable deposition of redox catalysts with controllable surface properties holds promise for developing further, tailored photocatalysts for various solar energy conversion applications beyond aerobic photooxidation of organic pollutants (e.g., water splitting or upgrading of low-cost chemical feedstock to high-value compounds).

### 4. Experimental Section

**Colloid Synthesis by Laser Ablation in Water:** To generate the colloidal CuO<sub>x</sub> and FeO<sub>x</sub> nanoparticles, a nanosecond laser system (Rofin Sinar RSM100D, 1064 nm with 30 W laser power and 6 mJ pulse energy at a repetition rate of 5 kHz) and a continuous ablation flow chamber were used.<sup>[20]</sup> The targets were generated from CuO (Sigma-Aldrich, grain size <10 μm, 98% purity) and Fe<sub>2</sub>O<sub>3</sub> (Sigma-Aldrich, grain size <5 μm, ≥99% purity) micropowders. These powders were pressed with 100 kN for 10 and 45 min in case of CuO and Fe<sub>2</sub>O<sub>3</sub>, respectively. The mechanical stability was improved by a sintering process for 12 h at 1000 °C. For particle generation, the laser beam was focused and moved in a spiral pattern on the powder-pressed targets using a galvanometric scanner system (F-Theta lens  $f = 63$  mm and working distance from lens surface to the target of 75 mm (optimum in nanoparticle productivity)). The pure water (Milli-Q, 18.2 MΩ cm) with a liquid layer of 6 mm was pumped with a flow rate of 50 mL min<sup>-1</sup> through the chamber.

Average size determination of the colloidal CuO<sub>x</sub> and FeO<sub>x</sub> particles was conducted with the analytical disk centrifuge (CPS DC2400) at a centrifugation speed of 24 000 rpm up to the lowest detection limit of a nanoparticle diameter of 3 nm. To this end, the samples were centrifuged against a saccharose gradient and an external standard (PVC particles at 0.238 μm), using a sample volume of 0.1 mL. The intensity data of the instrument were converted into weight-, number-, and surface-weighted size distributions. A log-normal fit was applied to each distribution and the expected value  $x_{\text{mean}}$  of the log-normal fit was taken as average particle diameter.

The IEPs of the colloids and the TiO<sub>2</sub>(A) substrate were determined by zeta potential measurements at several pH values with a Malvern Zetasizer Nano ZS in a capillary cell (750 μL) in combination with an autotitrator (MPT-2, Malvern).

**Electrostatically Directed Colloidal Deposition:** The substrate for colloidal deposition was anatase TiO<sub>2</sub>(A) powder consisting of ≈0.2–1 μm sized aggregates of smaller crystallites (average size of 15 nm obtained by Scherrer formula from a powder XRD pattern). It was obtained by heating a commercial TiO<sub>2</sub> powder (Hombikat UV 100, Sachtleben, Germany) at

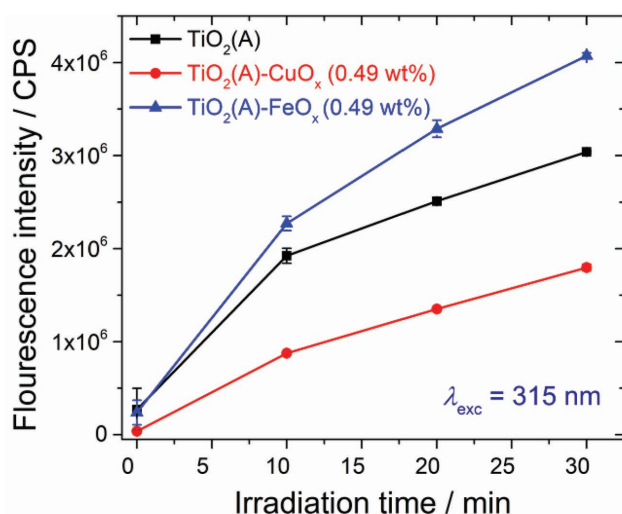


**Figure 6.** The formation of reactive •OH radicals followed as the time dependence of the hydroxyterephthalic acid fluorescence intensity at  $\lambda_{\text{max}} = 425$  nm.

400 °C in air for 4 h in order to improve its crystallinity and photoactivity. Colloidal deposition on the TiO<sub>2</sub>(A) support was performed by adjusting the pH value (using 0.1 M nitric acid or 0.1 M NaOH) of both the TiO<sub>2</sub>(A) suspension in water and the CuO<sub>x</sub> or FeO<sub>x</sub> colloidal solutions to 6, and mixing the respective volume of the colloidal solutions with the TiO<sub>2</sub>(A) suspension. After the deposition of the nanoparticles on the support surface and after sedimentation, the supernatant was removed, and the obtained powders were dried overnight at 60 °C in an oven. The loading efficiency (LE) was estimated from the UV–vis absorption spectra of the colloidal solutions and of the supernatant after the deposition. It was calculated as  $LE = (A_{300, \text{colloid}} - A_{300, \text{supernatant}}) / A_{300, \text{colloid}}$ , where  $A_{300, \text{colloid}}$  and  $A_{300, \text{supernatant}}$  were the absorbance at 300 nm of the colloidal solution and supernatant, respectively. The actual mass loading (wt%) was then calculated as the nominal (theoretical) mass loading multiplied by LE.

**Photocatalyst Characterization:** XRD patterns were recorded in transmission geometry using a STOE STADI-P diffractometer with Cu K $\alpha_1$  radiation (1.54060 Å), operating at 40 kV and 40 mA and equipped with a DECTRIS MYTHEN 1 K strip detector.

The UV–vis absorption spectra were measured by diffuse reflectance spectroscopy with a Perkin Elmer Lambda 650 UV–vis spectrophotometer with a praying mantis setup. The background reflectance of BaSO<sub>4</sub> (reference) was measured earlier. The evaluation of the data obtained was conducted according to the Kubelka–Munk function  $F(R_{\infty})$  as  $F(R_{\infty}) = (1 - R_{\infty})^2 / 2R_{\infty}$ , with  $R_{\infty}$  being the diffuse reflectance of the sample relative to the reflectance of a standard (BaSO<sub>4</sub>).

Scanning electron microscopy investigations were performed using LEO-1550 FE-SEM (Zeiss) with the EDX spectroscopy System Inca Energy from Oxford Instruments with the liquid nitrogen cooled Si(Li) solid-state detector and the software Inca 4000, Issue 17b.

TEM of CuO<sub>x</sub> and FeO<sub>x</sub> colloids was carried out on a Philips CM12 microscope. The catalyst dispersions were dropped on a carbon-coated copper grid and dried in air. TEM images of composite photocatalysts were acquired using an image-side aberration corrected FEI Titan 80-300 microscope operated at 80 kV equipped with Gatan GIF Quantum energy filter. This system was used for acquisition of high-resolution TEM images for morphology determination (particle size, crystallinity), and EELS and EFTEM. EELS was applied to determine the integral element composition of the nanoparticles and EFTEM to map the elemental distribution. In addition, the EELS/EFTEM analysis was accompanied by EDX spectroscopy using a Philips CM20 TEM operated at 200 kV (equipped with a EDAX Si:Li detector). Prior to the TEM investigations, the (powder) samples were dispersed in ethanol solution using a supersonic bath and drop casted to holey carbon grids.

Solid-state photoluminescence spectra were recorded using a Horiba Jobin Yvon Fluorolog spectrophotometer with the excitation wavelength of 340 nm (slit: 10 nm; integration time: 0.1 s).

XPS measurements were performed with a VersaProbe II (Ulvac-Phi, Chanhassen, USA). The CuO<sub>x</sub>-TiO<sub>2</sub> and FeO<sub>x</sub>-TiO<sub>2</sub> samples were measured in powder form using an Al K $\alpha$  X-ray source and a pass energy of 23.5 eV. To correct measurement-related minor shifts, BEs of all XPS spectra were referenced to a copper sample (measured BE: 930.87 eV; reference BE: 932.67 eV; shift for correction of all BEs: +1.80 eV).<sup>[21]</sup> Deconvolution of the spectra was conducted using Casa XPS. For elemental peaks an asymmetric Lorentzian was used, while oxidation peaks were fitted by symmetric Gaussian–Lorentzian function for peak deconvolution. During the fitting process, peak shifts of FeO<sub>x</sub> peaks with respect to elementary iron as well as doublet splitting were kept constant in line with the literature ( $\Delta BE_{Fe(II)} = 3.3$  eV;  $\Delta BE_{Fe(III)} = 4.0$  eV;  $\Delta BE_{\text{Doublet}} = 13.6$  eV).<sup>[14]</sup> In case of CuO<sub>x</sub> and very small peak splitting of elementary Cu and Cu<sub>2</sub>O, both peaks were constrained between 932.3 and 932.67 eV, while CuO peak shift was referenced on elementary copper with  $\Delta BE_{Cu(II)} = 1$  eV ( $\Delta BE_{\text{Doublet}} = 19.75$  eV).<sup>[15]</sup>

**Photocatalytic Experiments:** The photocatalytic degradation of 2,4-D was investigated. A solution of the pollutant (2,4-D,  $2.5 \times 10^{-4}$  mol L<sup>-1</sup>, 25 mL) was added into a borosilicate glass cell with the photocatalyst (25 mg; 1 g L<sup>-1</sup>). The obtained suspension was sonicated in the dark for 1 min. Subsequently, the reaction cell was fixed under a US-800 solar simulator (150 W xenon lamp, UNNASOL GmbH, Germany;  $\approx 17$  mW cm<sup>-2</sup> incident

light power density) equipped with a heat-absorbing filter (HA03, Hebo) and stirred magnetically in the dark for 4 min. The photocatalytic degradation was investigated for 90 min. Samples were taken at regular intervals, collected in the dark, and then filtered through a micropore filter (Sarstedt, 0.20  $\mu$ m). A typical pH value of the degradation slurry was between 3.5 and 4.2 during the degradation experiments. The concentration changes of 2,4-D were followed by UV–vis spectroscopy using a Cary 60 spectrometer.

The efficiency of hydroxyl radical generation was estimated by measuring the photocatalytic conversion of TA to TAOH. Photocatalysts were irradiated in TA solution ( $6 \times 10^{-3}$  mol L<sup>-1</sup> TA, 0.01 M HCl, pH set to 6) for 30 min. Samples were collected at 10 min intervals. In the reaction of nonfluorescent TA with hydroxyl radicals, the formation of TAOH can be monitored by emission spectra measurements. TAOH shows a broad emission band at  $\lambda_{\text{max}} = 425$  nm when excited at  $\lambda_{\text{exc}} = 315$  nm. Fluorescence spectra were measured using a FluoroLog-3 (Horiba Jobin Yvon) spectrofluorometer with a 1 cm quartz cuvette (slit: 1 nm; integration time: 0.1 s).

The average values of degradation and TAOH formation and the standard deviations ( $\sigma$ ) were calculated from at least three experiments. The error bars were constructed using 2 $\sigma$  values (confidence interval of  $\approx 95\%$ ).

## Supporting Information

Supporting Information is available from the Wiley Online Library or from the author.

## Acknowledgements

S.K. and P.P. contributed equally to this work. Financial support by the EU-FP7 Grant “4G-PHOTOCAT” (Grant No. 309636) and by the DFG (SFB/TRR 234 “CataLight”) is gratefully acknowledged. The authors thank the Sachtleben company for providing Hombikat UV 100 and the Center of Analytics on the Nanoscale (ICAN) for TEM measurements. S.K. and G.M. thank the German Federal Ministry of Education and Research (BMBF) within the young investigator competition NanoMatFutur (project INNOKAT, FKZ 03  $\times$  5523) for financial support and P. Wagener for fund acquisition.

## Conflict of Interest

The authors declare no conflict of interest.

## Keywords

colloidal deposition, laser ablation, nanoparticles, photocatalysis, titanium dioxide

Received: October 2, 2018

Revised: December 6, 2018

Published online:

- [1] a) H. Kisch, *Angew. Chem., Int. Ed.* **2013**, 52, 812; b) H. Kisch, *Semiconductor Photocatalysis: Principles and Applications*, Wiley-VCH, Weinheim **2015**; c) J. Cai, J. Shen, X. Zhang, Y. H. Ng, J. Huang, W. Guo, C. Lin, Y. Lai, *Small Methods* **2018**, <https://doi.org/10.1002/smt.201800184>; d) J. Low, C. Jiang, B. Cheng, S. Wageh, A. A. Al-Ghamdi, J. Yu, *Small Methods* **2017**, 1, 1700080; e) K. Ithisuphalap, H. Zhang, L. Guo, Q. Yang, H. Yang, G. Wu, *Small Methods* **2018**, <https://doi.org/10.1002/smt.201800352>.

- [2] a) B. Kraeutler, A. J. Bard, *J. Am. Chem. Soc.* **1978**, *100*, 4317; b) A. Mills, *J. Chem. Soc., Chem. Commun.* **1982**, 367; c) B. Ohtani, K. Iwai, S.-i. Nishimoto, S. Sato, *J. Phys. Chem. B* **1997**, *101*, 3349; d) P. V. Kamat, *J. Phys. Chem. Lett.* **2012**, *3*, 663; e) J. Yang, D. Wang, H. Han, C. Li, *Acc. Chem. Res.* **2013**, *46*, 1900; f) R. Li, F. Zhang, D. Wang, J. Yang, M. Li, J. Zhu, X. Zhou, H. Han, C. Li, *Nat. Commun.* **2013**, *4*, 1432.
- [3] a) H. Gerischer, A. Heller, *J. Phys. Chem.* **1991**, *95*, 5261; b) H. Gerischer, A. Heller, *J. Electrochem. Soc.* **1992**, *139*, 113.
- [4] a) Y. Tamaki, A. Furube, M. Murai, K. Hara, R. Katoh, M. Tachiya, *J. Am. Chem. Soc.* **2006**, *128*, 416; b) L. Jing, Y. Cao, H. Cui, J. R. Durrant, J. Tang, D. Liu, H. Fu, *Chem. Commun.* **2012**, 48, 10775.
- [5] a) D. W. Bahnemann, J. Mönig, R. Chapman, *J. Phys. Chem.* **1987**, *91*, 3782; b) D. Hufschmidt, D. Bahnemann, J. J. Testa, C. A. Emilio, M. I. Litter, *J. Photochem. Photobiol. A* **2002**, *148*, 223; c) A. A. Ismail, D. W. Bahnemann, *J. Phys. Chem. C* **2011**, *115*, 5784.
- [6] a) H. Irie, K. Kamiya, T. Shibamura, S. Miura, D. A. Tryk, T. Yokoyama, K. Hashimoto, *J. Phys. Chem. C* **2009**, *113*, 10761; b) H. Yu, H. Irie, Y. Shimodaira, Y. Hosogi, Y. Kuroda, M. Miyauchi, K. Hashimoto, *J. Phys. Chem. C* **2010**, *114*, 16481; c) X. Qiu, M. Miyauchi, K. Sunada, M. Minoshima, M. Liu, Y. Lu, D. Li, Y. Shimodaira, Y. Hosogi, Y. Kuroda, K. Hashimoto, *ACS Nano* **2012**, *6*, 1609; d) M. Liu, R. Inde, M. Nishikawa, X. Qiu, D. Atarashi, E. Sakai, Y. Nosaka, K. Hashimoto, M. Miyauchi, *ACS Nano* **2014**, *8*, 7229; e) S. J. A. Moniz, S. A. Shevlin, X. An, Z.-X. Guo, J. Tang, *Chem. Eur. J.* **2014**, *20*, 15571; f) S. J. A. Moniz, J. Tang, *ChemCatChem* **2015**, *7*, 1659.
- [7] a) S. Neubert, P. Pulisova, C. Wiktor, P. Weide, B. Mei, D. A. Guschin, R. A. Fischer, M. Muhler, R. Beranek, *Catal. Today* **2014**, *230*, 97; b) S. Neubert, D. Mitoraj, S. A. Shevlin, P. Pulisova, M. Heimann, Y. Du, G. K. L. Goh, M. Pacia, K. Kruczala, S. Turner, W. Macyk, Z. X. Guo, R. K. Hocking, R. Beranek, *J. Mater. Chem. A* **2016**, *4*, 3127; c) J. Patzsch, J. N. Spencer, A. Folli, J. Z. Bloh, *RSC Adv.* **2018**, *8*, 27674; d) J. Patzsch, J. Z. Bloh, *Catal. Today* **2018**, *300*, 2.
- [8] J. Z. Bloh, *J. Phys. Chem. C* **2017**, *121*, 844.
- [9] T. Arai, M. Horiguchi, M. Yanagida, T. Gunji, H. Sugihara, K. Sayama, *J. Phys. Chem. C* **2009**, *113*, 6602.
- [10] a) V. Amendola, P. Riello, S. Polizzi, S. Fiameni, C. Innocenti, C. Sangregorio, M. Meneghetti, *J. Mater. Chem.* **2011**, *21*, 18665; b) V. Amendola, M. Meneghetti, *Phys. Chem. Chem. Phys.* **2013**, *15*, 3027; c) D. Zhang, B. Gökce, S. Barcikowski, *Chem. Rev.* **2017**, *117*, 3990; d) J. Zhang, J. Claverie, M. Chaker, D. Ma, *ChemPhysChem* **2017**, *18*, 986; e) G. Marzun, H. Bönemann, C. Lehmann, B. Spliethoff, C. Weidenthaler, S. Barcikowski, *ChemPhysChem* **2017**, *18*, 1175.
- [11] a) E. Vahabzadeh, M. J. Torkamany, *J. Cluster Sci.* **2014**, *25*, 959; b) B. K. Pandey, A. K. Shahi, J. Shah, R. K. Kotnala, R. Gopal, *Appl. Surf. Sci.* **2014**, *289*, 462.
- [12] G. Marzun, C. Streich, S. Jendrzey, S. Barcikowski, P. Wagener, *Langmuir* **2014**, *30*, 11928.
- [13] N. Nie, L. Zhang, J. Fu, B. Cheng, J. Yu, *Appl. Surf. Sci.* **2018**, *441*, 12.
- [14] D. D. Hawn, B. M. DeKoven, *Surf. Interface Anal.* **1987**, *10*, 63.
- [15] N. S. McIntyre, M. G. Cook, *Anal. Chem.* **1975**, *47*, 2208.
- [16] J. Lam, D. Amans, C. Dujardin, G. Ledoux, A.-R. Allouche, *J. Phys. Chem. A* **2015**, *119*, 8944.
- [17] L. Trotochaud, T. J. Mills, S. W. Boettcher, *J. Phys. Chem. Lett.* **2013**, *4*, 931.
- [18] T. Hirakawa, Y. Nosaka, *Langmuir* **2002**, *18*, 3247.
- [19] a) H. Harada, T. Sakata, T. Ueda, *J. Am. Chem. Soc.* **1985**, *107*, 1773; b) J. Ryu, W. Choi, *Environ. Sci. Technol.* **2008**, *42*, 294; c) B. Ohtani, *J. Photochem. Photobiol. C* **2010**, *11*, 157.
- [20] S. Barcikowski, V. Amendola, G. Marzun, C. Rehbock, S. Reichenberger, D. Zhang, B. Gökce, *Handbook of Laser Synthesis of Colloids*, Universität Duisburg-Essen **2016**.
- [21] M. P. Seah, M. T. Anthony, *Surf. Interface Anal.* **1984**, *6*, 230.